

10

Magnetic Mineralogy of Meteoritic Metal: Paleomagnetic Evidence for Dynamo Activity on Differentiated Planetesimals

RICHARD J. HARRISON, JAMES F. J. BRYSON, CLAIRE I. O. NICHOLS,
AND BENJAMIN P. WEISS

10.1 Introduction

Many meteorite parent bodies experienced large-scale melting due to heating from short-lived radionuclides during the early solar system, leading to differentiation and the formation of a metallic core overlain by a silicate mantle (Hevey and Sanders, 2006). It has recently been realized that advective motion of these cores likely generated dynamo magnetic fields (Weiss *et al.*, 2008) that then imprinted magnetization in the overlying silicate rocks. The magnetic histories of planetesimals therefore provide important constraints on planetesimal thermal histories and on the physics of dynamo generation in a small-body regime not represented by planetary dynamos active in the solar system today.

The only known samples of planetary cores are the iron meteorites and perhaps also stony-iron meteorites. Nearly all meteoriticists have previously discounted the possibility that these lithologies could record a core dynamo for two major reasons. First, if these samples are from a metallic core covered by a thick, insulating silicate mantle, the core should be nearly isothermal due to metal's high thermal conductivity, such that by the time that core cools to temperatures sufficiently low that it could become permanently magnetized, any dynamo activity may have long since decayed away (Cisowski, 1987). Secondly, the large grain size, intergrown texture, and poorly understood magnetic properties of the metal phases, as well as their extended history of subsolidus recrystallization, has meant that it has been difficult to relate their observed magnetization to the presence of an ancient planetary magnetic field (Brecher and Albright, 1977). This is because experimental techniques in the field of paleomagnetism have been largely developed for silicate rocks like those found on Earth. Here, we describe recent breakthroughs in our understanding of the rock magnetic properties and remanent magnetization of meteoritic metal and its implications for the magnetic history, differentiation, and structures of stony-iron and iron meteorite parent bodies.

Microstructural and geochemical studies of meteoritic metal have been instrumental in shaping our current views of differentiated planetesimals, providing constraints on their cooling rate, their size, the timing of their differentiation and their fractional crystallization and impact histories (Goldstein *et al.*, 2009a; Kleine *et al.*, 2009). The characteristic Widmanstätten microstructure, familiar to anyone who has looked at a polished and etched section of an iron meteorite with the naked eye, hides a nanoscale complexity that is revealed only with high-resolution electron microscopy – a legacy of stranded diffusion profiles, metastability, martensitic transformations, chemical segregation, and ordering during slow cooling of the parent body. Despite our wealth of knowledge about these nanoscale features, their magnetic properties have remained largely unstudied. From a paleomagnetic perspective, this is perhaps not surprising: the bulk magnetic properties of meteoritic metal are dominated by ubiquitous kamacite, a multi-domain soft ferromagnetic material that makes a notoriously poor paleomagnetic recorder. Recently, however, our ideas about the paleomagnetic potential of meteoritic metal have shifted dramatically (Uehara *et al.*, 2011; Bryson *et al.*, 2014a). The seeds of this change began with the discovery of tetrataenite – an atomically ordered tetragonal form of $\text{Fe}_{0.5}\text{Ni}_{0.5}$ with ultra-high paleomagnetic stability (Néel *et al.*, 1964; Lewis *et al.*, 2014). Although the existence of tetrataenite has been recognized in meteoritic metal since the 1980s (Clarke and Scott, 1980; Wasilewski, 1988), its occurrence in spatially restricted “rims” and “cloudy zones,” often only a few micrometers wide, means its paleomagnetic significance has only recently been revealed using high-resolution magnetic imaging (Bryson *et al.*, 2014b). Given that hypothesized formation mechanisms for some classes of iron and stony-iron meteorites suggest they may have been exposed to a core dynamo (Tarduno *et al.*, 2012), there is now renewed motivation to study the mineral magnetism of meteoritic metal, and discover what its paleomagnetic signals can tell us about the thermochemical history of differentiated planetesimals.

This chapter begins by reviewing recent work that has transformed our understanding of the magnetic properties of meteoritic metal, focusing on the dramatic variations in magnetic behavior in zoned taenite revealed by X-ray magnetic imaging and electron holography. Next, we describe the nanopaleomagnetic signals recorded by the metal component of the main-group pallasites, and what they reveal about the history of dynamo activity on the pallasite parent body. Finally, we look forward to the new opportunities provided by these emerging methods, and identify potential targets for future study, focusing on those iron meteorite groups where paleomagnetism could contribute most to our understanding of differentiated planetesimals.

10.2 Mineral Magnetism of Meteoritic Metal

10.2.1 Summary of Microstructural Changes in Zoned Taenite

The microstructural evolution of zoned taenite has been studied in detail by Yang, Scott, Goldstein, and many others (Yang *et al.*, 1997a), and will be summarized only briefly here. Our description focuses on the behavior of samples cooled at intermediate rates ($2\text{--}18\text{ K Myr}^{-1}$), which are most relevant to the pallasites. Samples that cooled more slowly (e.g. the mesosiderites) or more quickly (e.g. the IVA irons) display additional complexities in their chemical and magnetic behavior that are only just being discovered, and will not be discussed here. Zoned taenite results from the nucleation and growth of Fe-rich kamacite below $\sim 900\text{--}1000\text{ K}$, which causes Ni to be partitioned into the surrounding taenite. The Ni content immediately adjacent to kamacite reaches 50%, causing a rim of tetrataenite to form below 593 K (Figure 10.1a). Tetrataenite is a tetragonal form of $\text{Fe}_{0.5}\text{Ni}_{0.5}$ (L1_0 structure) in which Fe and Ni atoms order onto alternating $\{100\}$ layers. The tetrataenite rim ends abruptly when the Ni content drops below $\sim 47\%$ Ni, corresponding to the maximum extent of the single-phase tetrataenite stability field (Yang *et al.*, 1996). Beyond the tetrataenite rim, the bulk Ni content continues

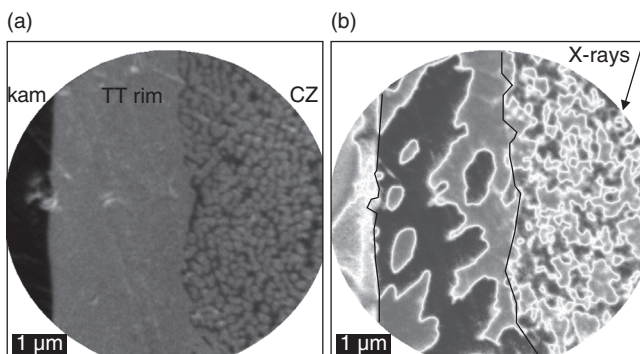


Figure 10.1 (a) Chemical map of zoned taenite in the Marjalahti pallasite. Image was obtained using XPEEM with linearly polarised X-rays tuned to the Ni L3 absorption edge (854 eV). Brightness is proportional to the Ni concentration. The dark region (left) is Ni-poor kamacite (kam). The bright region (central) is the tetrataenite rim (TT rim). The mixed region (right) is the coarse cloudy zone (CZ), consisting of bright tetrataenite islands within a dark Fe-rich matrix. (b) Magnetization map of the region in (a) obtained using XPEEM with circularly polarised X-rays tuned to the Fe L3 absorption edge (707 eV). Blue and red colors indicate positive and negative projections of the in-plane surface magnetisation along the incident X-ray beam direction (arrow), respectively. Black lines are guides to the eye, showing the positions of the kam/TT rim and TT-rim/CZ boundaries. A black and white version of this figure will appear in some formats. For the colour version, please refer to the plate section.

to decrease and the system enters a two-phase region containing tetrataenite “islands” embedded in an Fe-rich “matrix” (Figure 10.1a). This two-phase region is referred to as the “cloudy zone” (CZ). Although the term “island” is often used to describe the tetrataenite component of the CZ, this morphology may be an artefact of two-dimensional sectioning: individual tetrataenite islands likely form an interconnected network in three dimensions in the coarse regions of the CZ close to the tetrataenite rim, with a transition to isolated islands occurring further from the interface, driven by the changing proportions of island and matrix phases (Yang *et al.*, 1997a). The identity of the matrix phase has been the subject of much debate (Reuter *et al.*, 1988; Yang *et al.*, 1997a; Leroux *et al.*, 2000; Goldstein *et al.*, 2009a), and we will return to this discussion in Section 10.2.3. The morphology of the CZ is consistent with formation via spinodal decomposition, whereby the system becomes unstable with respect to sinusoidal fluctuations in composition below a critical spinodal temperature (T_s). On cooling below T_s , a period of rapid growth in the amplitude of compositional fluctuations is followed by a more prolonged period of coarsening. Tetrataenite islands are largest immediately adjacent to the tetrataenite rim. Their size correlates inversely with cooling rate (varying from ~500 nm in the most slowly cooled mesosiderites to ~10 nm in the most rapidly cooled IVA meteorites) (Yang *et al.*, 1997b; Goldstein *et al.*, 2009b). The size of the tetrataenite islands decreases systematically with increasing distance from the tetrataenite rim, reflecting the lower local Ni content and the corresponding lower T_s . We will demonstrate below that regions with small island sizes have distinct magnetic properties from those with large island sizes and, on that basis, make a distinction between “coarse CZ” and “fine CZ.” When the local Ni content is less than 25%, taenite partially transforms to a bcc structure via a martensitic transformation, followed by chemical segregation to form plessite (an intergrowth of bcc kamacite and fcc taenite and/or tetrataenite) (Zhang *et al.*, 1993; Goldstein and Michael, 2006).

10.2.2 X-ray Photo-emission Electron Microscopy

X-ray photo-emission electron microscopy (XPEEM) is a synchrotron X-ray magnetic imaging technique that yields quantitative maps of surface magnetic moment with a typical field-of-view of 5 μm and spatial resolution down to 30 nm (Locatelli and Bauer, 2008). Given the characteristic length scales of the key microstructural features in zoned taenite, XPEEM is ideally suited to reveal the corresponding changes in magnetic microstructure (Figure 10.1b). XPEEM works by shining an intense beam of soft X-rays onto a polished surface under ultra-high vacuum conditions. The energy of the beam is tuned to the absorption edge of the element of interest (either Fe or Ni in the case of meteoritic metal) and

the polarization state of the beam is controlled by an undulator insertion device. As X-rays are absorbed by the sample, secondary electrons escaping from the top ~ 5 nm of the surface are accelerated through a series of electron lenses and focused to a high-resolution image. Mechanical polishing, combined with exposure to air, induces a structural and chemical change in the upper ~ 100 nm of the sample surface (Bryson *et al.*, 2014a, 2014b). Given the surface sensitivity of XPEEM, this layer must be removed by Ar-ion sputtering, thereby exposing the unaltered metal underneath. Sputtering is performed *in situ* under ultra-high vacuum conditions to prevent further oxidation of the surface prior to measurement. Sputtering can introduce unwanted topography into the sample surface, caused by differential etching of Fe-rich and Ni-rich phases. This effect is minimised by gradually reducing the accelerating voltage of the Ar-ion beam over a period of several hours. The high coercivity of the CZ, which is directly linked to the underlying chemical ordering, prevents magnetic structures from being altered by the sputtering. XPEEM detects the magnetic moment of the sample surface via the mechanism of X-ray magnetic circular dichroism (XMCD). Circularly polarized X-rays interact with the spin and orbital angular momentum of a 2p electron as it is excited into an available 3d state. Transfer of angular momentum from the X-ray to the electron makes the absorption process dependent on the orientation of net spin (i.e. magnetic moment) with respect to the incoming X-ray beam. To isolate the magnetic contribution to the absorption signal, images are taken with both left and right circular polarization. The difference between the two images, normalized by their sum, is proportional to the component of magnetic moment parallel to the incoming X-ray beam. X-rays hit the sample at a glancing angle of 16° to the surface, so the XPEEM images are dominated by the in-plane component of magnetic moment. Blue and red colors are used to depict positive and negative projections along the X-ray direction, respectively, with white indicating either zero moment or a moment that is perpendicular to the X-ray beam.

10.2.3 Magnetic Microstructures of Zoned Taenite

XPEEM images of kamacite show large-scale conventional magnetic domain structures. Far from the interface with tetrataenite, kamacite domains are typically elongated with widths in the range $0.5\text{--}5\text{ }\mu\text{m}$ (Figure 10.2). Domain walls are moved easily by magnetic fields $\ll 100$ mT. Due to the soft ferromagnetic nature of kamacite, magnetic moments remain parallel to the sample surface in order to minimize the local demagnetizing energy. Domains in the tetrataenite rim differ from those in kamacite in several fundamental ways (Figure 10.2). The domains are very much smaller, roughly corresponding to the width of the rim itself, and they are much more stable with respect to magnetic fields. Out-of-plane

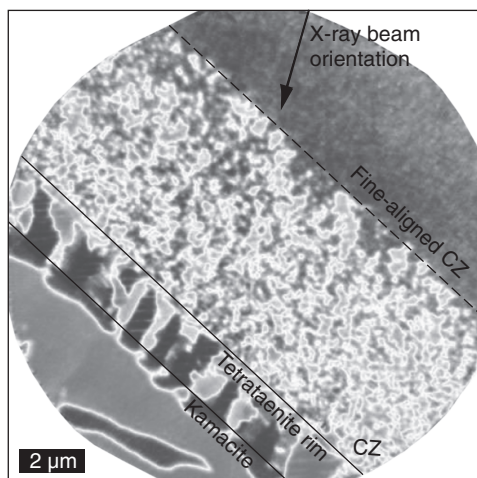


Figure 10.2 15- μm -field-of-view magnetization map of zoned taenite in the Imilac pallasite (Bryson *et al.*, 2015), obtained using XPEEM with circularly polarised X-rays tuned to the Fe L3 absorption edge (707 eV). Blue and red colors indicated positive and negative projections of the in-plane surface magnetisation along the incident X-ray beam direction (arrow), respectively. The boundaries between the kamacite, tetrataenite rim and CZ are marked as solid black lines, and the boundary between the CZ and fine-aligned CZ is marked as a dashed black line. Note the coarser and more conventional domains visible within the kamacite, compared to the finer and more complex looking domains within the tetrataenite. Note also the sudden onset (in this case, at least) of uniform magnetization in the fine CZ, indicating a fundamental change from an exchange-spring regime to a rigidly coupled regime. The precise nature of the change in the underlying nanostructure that drives this transition is not yet known. Reproduced from Bryson *et al.* (2015). A black and white version of this figure will appear in some formats. For the colour version, please refer to the plate section.

magnetization is observed in the rim, with magnetic moments and domain walls directed parallel or antiparallel to the three $\langle 100 \rangle$ crystallographic directions of the parent taenite. These directions correspond to three possible choices of tetrataenite's tetragonal c axis, which are in turn normal to the three possible $\{100\}$ orientations of Fe–Ni layering (Lewis *et al.*, 2014). The high magnetocrystalline anisotropy of tetrataenite means that magnetic moments remain rigidly fixed to the c axes, even when they point out of the sample plane. This observation is critical: it means that the natural remanent state of tetrataenite is preserved during sample preparation, despite the creation of a surface. It also means that the XMCD signals corresponding to each of the six possible magnetization states of tetrataenite can be extracted from a histogram analysis of rim intensities, without the need for additional crystallographic orientation information (a crucial step in quantifying the XPEEM images – see Section 10.3). There is evidence of

significant domain wall interaction between kamacite and the tetrataenite rim, with domains in the rim “bleeding” across into the kamacite. This is easily explained by domains in the soft kamacite adjusting themselves to the more stable domain structures in the rim.

A dramatic reduction in domain size relative to the tetrataenite rim is observed in the CZ (Figure 10.1b, 10.2). Domains in the CZ form an interlocking pattern of positive and negative XMCD signals separated by meandering domain walls. A universal feature is the lack of significant interaction between the CZ domain pattern and that of the tetrataenite rim, suggesting that these domain patterns formed independently and that the magnetism of the CZ is not unduly influenced by interaction with the surrounding metal. The heterogeneous magnetic state of the CZ is consistent with the presence of all six possible *c* axes of tetrataenite (in varying proportions), implying that the 3D network of interconnected tetrataenite regions is cross-cut on a fine scale by crystallographic twin walls separating regions of distinct crystallographic orientation. The length scale of the magnetic domains is typically ~1–5 times the tetrataenite island size (Bryson *et al.*, 2014b). Hence, regions of strong XMCD signal encompass both the tetrataenite islands and the surrounding matrix. This observation demonstrates that the matrix phase is ferromagnetic, casting doubt on the currently accepted interpretation that the matrix is composed of antitaenite, a low-spin paramagnetic polymorph of taenite that has been identified in Mössbauer spectra of bulk Fe–Ni meteorites (Rancourt and Scorzelli, 1995; Rancourt *et al.*, 1999; Dos Santos *et al.*, 2014). Bryson *et al.* (2014a) presented several lines of evidence to support the hypothesis that the matrix phase is, instead, composed of atomically ordered Fe₃Ni (cubic L1₂ structure) – a phase that has not previously been identified in nature, but is predicted on the basis of density functional theory to be a soft ferromagnet at room temperature (James *et al.*, 1999): (i) electron diffraction patterns show only fcc phases present, ruling out a ferromagnetic bcc matrix phase; (ii) high-resolution elemental maps show that the Ni content of the matrix phase is ~25%; (iii) electron diffraction patterns taken in regions of the coarse CZ known to contain only two out of the three possible tetrataenite twin orientations show three distinct superlattice diffraction spots, consistent with the presence of Fe₃Ni; (iv) high-resolution magnetic induction maps of the coarse CZ obtained by electron holography are best explained by the presence of a soft ferromagnetic matrix; (v) the observed range of magnetic switching fields observed in the coarse CZ (~200–600 mT) is inconsistent with the behavior of isolated tetrataenite regions separated by a paramagnetic matrix, but can be reproduced in micromagnetic simulations involving exchange coupling between tetrataenite and a soft ferromagnetic matrix; (vi) thermodynamic modeling of the chemical and magnetic interactions that lead to the formation of tetrataenite predict that Fe₃Ni should form under similar

conditions (Dang *et al.*, 1995; Dang and Rancourt, 1996). Fe_3Ni does not currently appear in the low-temperature phase diagram of fcc Fe–Ni. If the presence of Fe_3Ni can be confirmed by chemical, structural, and magnetic analysis at sufficiently high spatial resolution, the phase diagram on which our current understanding of CZ formation is based will have to be revised considerably.

The physical picture of the CZ that emerges from these images is one of a hard–soft magnetic nanocomposite – a well-studied class of materials with magnetic properties controlled by exchange coupling across the interface between magnetically hard and soft phases (Asti *et al.*, 2004). The properties of such systems depend sensitively on the length scale of the soft phase compared to the magnetic exchange interaction length (~ 4 nm for Fe–Ni). According to such models, if the soft phase is large compared to the exchange length, then the switching field of the hard phase is lowered significantly by the influence of magnetic domain walls moving through the soft phase. For intermediate length scales, the switching field is lowered to a lesser degree and reversible domain wall processes in the soft phase can be observed (i.e. exchange spring behavior; Kneller and Hawig, 1991). When the soft phase is small compared to the exchange length, the formation of domain walls in the soft phase is no longer possible and the hard and soft phases become rigidly exchange coupled. In this case, the switching field approaches the intrinsic switching field of the hard phase, and the ability for adjacent hard regions to be magnetized in independent directions is suppressed.

XPEEM and electron holography images suggest that the coarse CZ is in the intermediate (exchange spring) regime and the fine CZ is in the rigidly coupled regime. As the tetrataenite island size decreases with increasing distance from the tetrataenite rim, a region of strongly aligned magnetization, with switching fields approaching the intrinsic coercivity of tetrataenite (1–2 T, depending on orientation), emerges in the fine CZ (Figure 10.2). In some cases this transition occurs quite suddenly, whereas in others it is more gradual. Due to the small length scale of the microstructure, the structural state of the fine CZ remains uncertain. There is some evidence that the matrix phase is less well ordered in the fine CZ than in the coarse CZ. It is also conceivable that the matrix of the fine CZ is the location of antitaenite. Because the high magnetic alignment observed in the fine CZ results from internal exchange coupling, rather than the action of an external field, no paleomagnetic information can be obtained from this region.

Beyond the (approximately) uniformly magnetized fine CZ, another dramatic change in magnetic properties occurs at the onset of plessite (Figure 10.3). Plessite forms via a two-step process. First, when taenite with $< 25\%$ Ni content cools below a critical martensite start temperature (Zhang *et al.*, 1993; Goldstein and Michael, 2006), a diffusionless martensitic transition occurs in which isochemical bcc laths form progressively out of the parent fcc taenite until the martensite finish

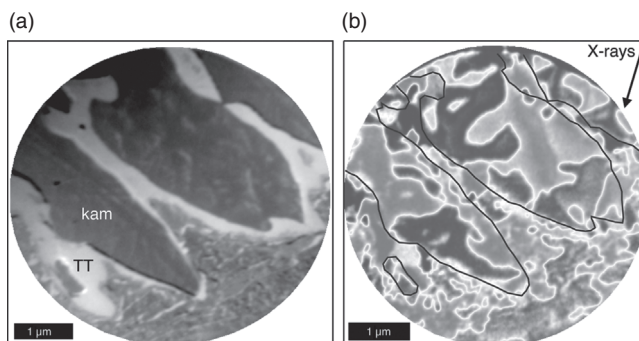


Figure 10.3 (a) Chemical map of plessite in the Marjalahti pallasite. Image was obtained using XPEEM with linearly polarised X-rays tuned to the Ni L3 absorption edge (854 eV). Brightness is proportional to the Ni concentration. Dark regions are laths of Ni-poor kamacite (kam) formed by martensitic transition. Bright regions are Ni-rich tetrataenite that form at the boundaries of the martensite laths. (b) Magnetization map of the region in (a) obtained using XPEEM with circularly polarised X-rays tuned to the Fe L3 absorption edge (707 eV). Blue and red colors indicate positive and negative projections of the in-plane surface magnetization along the incident X-ray beam direction (arrow), respectively. Black lines are guides to the eye, showing the kam/TT boundaries. Note the coarser and more conventional domains visible within the kamacite, compared to the finer and more complex looking domains within the tetrataenite. A black and white version of this figure will appear in some formats. For the colour version, please refer to the plate section.

temperature is reached. For continued slow cooling and sufficiently low bulk nickel contents, this transition will be followed by chemical segregation and ordering to form a two-phase mixture of Fe-rich kamacite laths separated by tetrataenite boundaries (Figure 10.3a). The magnetic state of plessite is dominated by multiple domains in many different orientations (Figure 10.3b). Our first detailed XPEEM images of plessite show much finer domain structures in the tetrataenite boundary regions in comparison to the kamacite laths, consistent with the behavior observed in the tetrataenite rim. Despite its multi-domain nature, magneto-optical studies of plessite indicate it has coercivity of remanence as high as 200 mT (Uehara *et al.*, 2011), making it a potential target for future paleomagnetic studies.

10.3 Dynamo Activity on the Main-group Pallasite Parent Body

10.3.1 Paleomagnetic Constraints on Origin of the Main-group Pallasites

The pallasites are stony-iron meteorites consisting of roughly 65% olivine, 30% Fe–Ni metal and 5% accessory phases (Figure 10.4). The vast majority (>90%) of

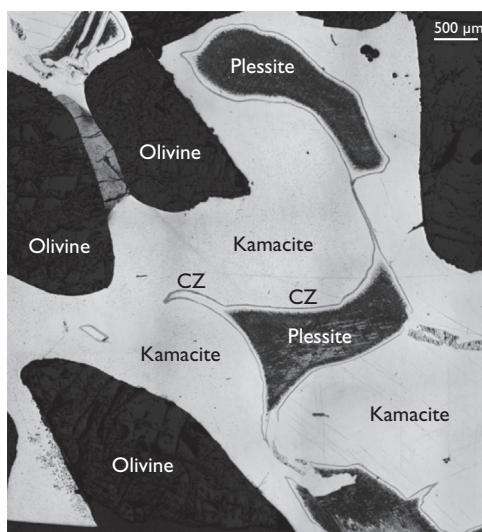


Figure 10.4 Reflected light optical micrograph of the Imilac pallasite. Sample was polished and etched with 2% nitric acid. Bright regions are swathing kamacite surrounding crystals of olivine (dark). Light grey line is the CZ, which surrounds localised regions of plessite.

pallasites belong to the main group (MG), which are considered to be derived from a single parent body. The formation of the MG pallasites and the nature of their parent body have been the subject of intense debate over many years (Boesenberg *et al.*, 2012). The intimate mixture of olivine and metal leads naturally to the concept that the pallasites formed close to the core–mantle boundary of a differentiated asteroid. Early theories, based on a close geochemical relationship between the MG pallasites and the IIIAB iron meteorites, suggested that these meteorites were derived from the same parent body and that the IIIAB irons are samples of its core (Wasson and Choi, 2003). However, this relationship has been questioned on the basis of incompatible cooling rates observed in the MG pallasites and the IIIAB irons (Yang *et al.*, 2010). Key issues with a core–mantle boundary origin for the MG pallasites include the difficulty in explaining why olivine crystals failed to separate gravitationally from the dense, low-viscosity metal liquid and how the diverse cooling rates ($2\text{--}18\text{ K Myr}^{-1}$) of the MG pallasites can be reconciled with the uniform cooling rates expected at the core–mantle boundary. Alternative formation mechanisms, suggesting a shallower impact origin for the pallasites, are now being widely discussed. In the context of this debate, paleomagnetism has emerged as a powerful tool, providing robust discrimination between core–mantle boundary and impact theories, and potentially even between alternative impact theories. In this section we begin by reviewing briefly the insights obtained recently through paleomagnetic analysis of olivine crystals extracted from the

MG pallasites (Tarduno *et al.*, 2012). We then demonstrate how quantitative analysis of XPEEM images of the CZ, outlined in Section 10.2, provides a new way to examine the evolution of dynamo activity on the MG pallasite parent body (Bryson *et al.*, 2015).

As noted in Section 10.2.1, past attempts at paleomagnetic analysis of metal-rich meteorites were confounded by the presence of soft ferromagnetic kamacite. Tarduno *et al.* (2012) circumvented this problem by focusing on the paleomagnetic signals recorded by single olivine crystals extracted from two MG pallasites (Imilac and Esquel). Although olivine itself is not ferromagnetic, a mixture of low-Ni iron and high-Ni taenite particles embedded within sulfide inclusions within the olivine make ideal remanence carriers, due both to their small size (which imparts single-domain or pseudo single-domain characteristics – a prerequisite for maintaining a faithful paleomagnetic signal) and the fact that they have been effectively protected from oxidation by encapsulation in the silicate. This single-crystal approach to paleomagnetism is well established in terrestrial studies, and is responsible for the earliest paleomagnetic evidence of dynamo activity on Earth at 3.45 Ga (Tarduno *et al.*, 2010). Alternating-field and thermal demagnetization were used to isolate the primary natural remanent magnetization (NRM) of magnetic inclusions within individual olivine crystals. By comparing the intensity of NRM with laboratory thermoremanent magnetization (TRM) acquired in a known magnetic field, the intensity of the field that magnetized olivine on the parent body was calculated to be 74 ± 8 μT and 122 ± 14 μT for the Imilac and Esquel pallasites, respectively. The NRM is carried by particles with blocking temperatures between 360 and 500 °C. Both the intensity of the magnetic field and the blocking temperature at which it was recorded are significant in terms of pallasite formation. Firstly, the only plausible explanation for fields of this size is the presence of a core dynamo on the MG pallasite parent body. This requires that a convecting liquid metal core was present at the same time the pallasites were cooling through 360–500 °C, ruling out a core–mantle origin (the core would have long since solidified by the time the core–mantle boundary reached these low temperatures). A combination of constraints, including the range of MG pallasite cooling rates, their lack of shock features (which rules out a near-surface origin), and the low blocking temperatures of NRM, lead to the conclusion that pallasites originated from the outer ~40 km of a differentiated planetesimal ~200 km in radius. On this basis, Tarduno *et al.* (2012) proposed that the pallasites formed during an impact between the pallasite parent body and another differentiated body, roughly one tenth the mass, which caused liquid metal from the impactor to intrude into the upper mantle of the pallasite parent body along downwardly intruding dykes.

Having established evidence for a core dynamo on the MG pallasite parent body, further paleomagnetic analysis of the pallasite metal can provide a window

on the temporal behavior of the magnetic field. Several key questions we might wish to address are: When did the dynamo start? How long did it last? Was the field dipolar or multipolar? Was the field directionally stable or reversing? What mechanism was driving convection in the core? Such questions are not only relevant to the specific case of MG pallasite parent body, but are of central importance in dynamo theory, and are highly relevant in developing an understanding of magnetic field generation on other asteroids, moons, and planets. Answering these questions requires detailed knowledge of how the magnetic field evolved with time. Below we describe how the unique properties of the CZ, and how it evolves during slow cooling, provide a time-resolved record of magnetic activity.

10.3.2 Nanopaleomagnetic Constraints on the Properties of the Pallasite Core Dynamo

As noted in Section 10.2.1, the CZ forms at progressively lower temperatures at increasing distances from the tetrataenite rim, a consequence of the decreasing local Ni content and the corresponding lower T_s (Goldstein *et al.*, 2009a). The magnetic state of the CZ can be biased by a magnetic field as it forms, resulting in a chemical-transformation remanent magnetization (CTRM). Given the slow cooling rates of the MG pallasites ($2\text{--}18\text{ K Myr}^{-1}$), CTRM is acquired at progressively later times with increasing distance from the tetrataenite rim, producing a time-resolved record of magnetic activity that can span several million years. High-resolution magnetic images of the CZ, such as those provided by XPEEM (Section 10.2.2), can therefore be used to investigate the temporal evolution of dynamo activity. This approach has been applied successfully to the metal in the Imilac and Esquel pallasites (Bryson *et al.*, 2015).

XPEEM images of the CZ in the Imilac and Esquel pallasites are qualitatively similar to those described in Section 10.2.3 (Figure 10.5a, d) but, importantly, they display a bias in the proportions of positive and negative signals. Departures from a random distribution of magnetization directions can be attributed to the influence of a strong magnetic field as the CZ was forming (Bryson *et al.*, 2014b). The spatial resolution of XPEEM images is not sufficient to allow the magnetization of individual tetrataenite islands to be determined, so a quantitative approach based on forward modeling of the XPEEM images is employed. Histograms of pixel intensity are extracted from discrete regions across the width of the CZ (Figure 10.5b, e). The shape of these histograms relates to the proportions of the six possible magnetic states of the tetrataenite islands, which in turn depend on both the intensity and direction of the field experienced by the CZ. The observed histograms are compared to synthetic histograms generated using known field

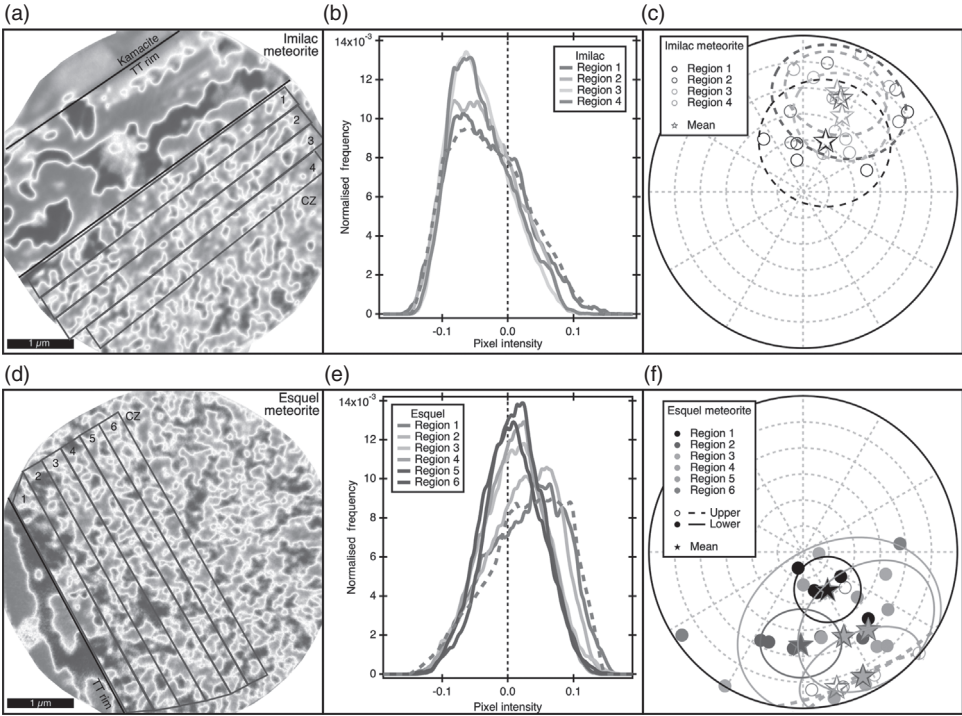


Figure 10.5 Representative 5- μm -field-of-view XPEEM images of the tetrataenite rim and CZ in the (a) Imilac and (d) Esquel meteorites. The CZ regions are marked in each image. Pixel intensity histograms of the (b) Imilac and (e) Esquel meteorites, corresponding to the regions in (a) and (d) respectively. Stereoplots of the directions of the field that best recreate the pixel intensity histograms for the (c) Imilac and (f) Esquel meteorites. The directions for all regions of the Imilac meteorite and regions 1–5 of the Esquel meteorite are self-consistent. The direction for region 6 of the Esquel meteorite displays a large degree of scatter. Modified after Bryson *et al.* (2015). A black and white version of this figure will appear in some formats. For the colour version, please refer to the plate section.

properties, and a least-squares optimization procedure is used to determine the intensity and direction of the field that minimize the difference between the observed and simulated histograms.

Four and six 450-nm-wide regions across the width of the CZ were studied in the Imilac and Esquel meteorites, respectively. The final directions for all regions of the Imilac meteorite and regions 1–5 of the Esquel meteorite are self-consistent; the directions from region 6 of the Esquel meteorite display a large degree of scatter (Figure 10.5c, f). The four regions from the Imilac meteorite display a roughly constant field intensity of $\sim 120\ \mu\text{T}$, implying this meteorite experienced a constant and intense field over time (Figure 10.6a). The Esquel meteorite displays

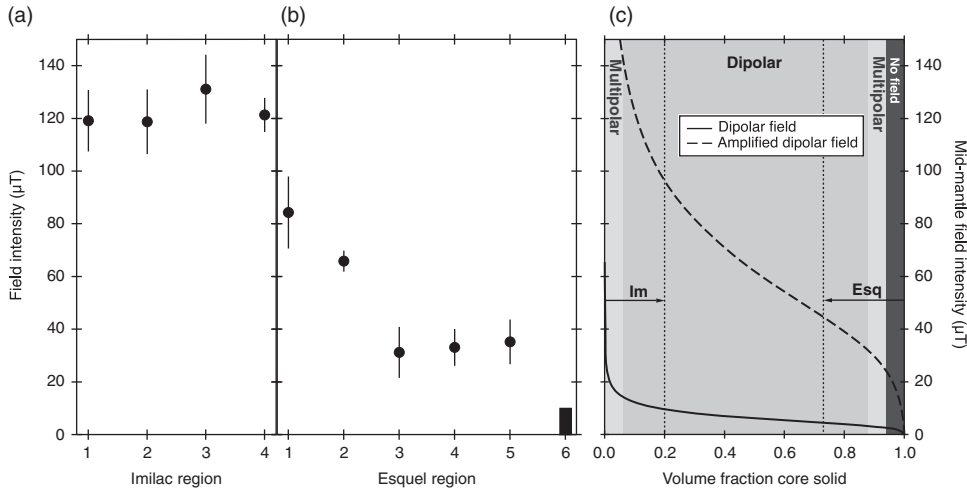


Figure 10.6 Intensity of the field over time for the (a) Imilac and (b) Esquel meteorite. The points and error bars correspond to the average and standard deviation in the best-fitting components for each region. The deduced field intensity of $<10 \mu\text{T}$ for region 6 of the Esquel meteorite is depicted as a black rectangle. The local CZ age decreases with increasing region number. (c) Results of the dynamo generation model. Solid line: dipolar field intensity; dashed line: amplified dipolar field. Red background: predicted dipolar period; blue background: predicted multipolar period; grey background: predicted zero-field period. Im and Esq correspond to the likely recording periods of the Imilac and Esquel meteorite, respectively. Modified after Bryson *et al.* (2015). A black and white version of this figure will appear in some formats. For the colour version, please refer to the plate section.

a very different trend, with the first two regions showing a sharp decrease in field intensity from $\sim 80 \mu\text{T}$ down to $30 \mu\text{T}$, followed by a plateau at this relatively weak value, before a final decay down to $\sim 0 \mu\text{T}$ in region 6 (Figure 10.6b). Each region corresponds to a time period of $\sim 1\text{--}2 \text{ Myr}$ (Bryson *et al.*, 2015).

To relate these trends to dynamo activity, the time that each meteorite recorded the field must be identified. By comparing models of the thermal evolution of the pallasite parent body (Tarduno *et al.*, 2012) and experimentally determined cooling rates (Yang *et al.*, 2010), both the original depths of the two meteorites and the time that their CZs started recording a magnetization were deduced. Both meteorites originate from approximately mid-way through their parent-body mantle ($\sim 38\text{--}45 \text{ km}$ depth) and started recording a magnetization during the early and late stages of core solidification, respectively (Figure 10.7). During this time, core convection could have been driven by the generation of a buoyant fluid created at depth in the core by the rejection of light elements (e.g. S) during inner core solidification, analogous to the present-day Earth (Fearn and Loper, 1981). To test this hypothesis,

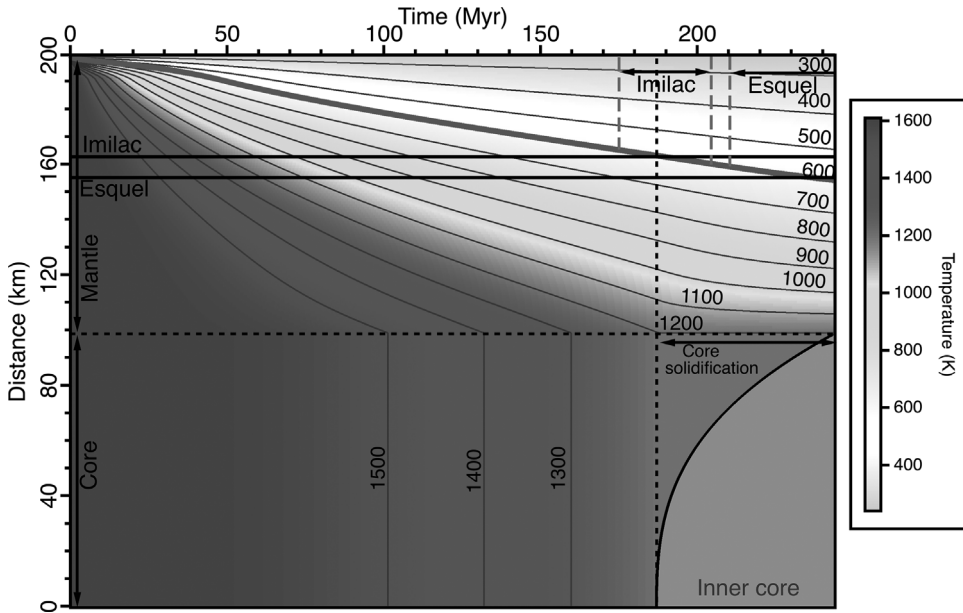


Figure 10.7 Cooling of a 200-km-radius body from an initial 1600-K isothermal state. The temperature is represented by the color. The solid red line marks the evolution of the depth of the CZ formation temperature (593 K). The inferred depths of the Imilac and Esquel meteorites are marked as horizontal black lines. The recording time period for each meteorite is marked as vertical grey dashed lines. The average depth of each meteorite reaches 593 K during core solidification. The evolution of the inner core radius is included. The core is isothermal at 1200 K across the entire period of solidification. Reproduced from Bryson *et al.* (2015). A black and white version of this figure will appear in some formats. For the colour version, please refer to the plate section.

the field generated by this process was calculated across the period of core solidification (Olson and Christensen, 2006). During the early stages, the field is predicted to be dipolar and relatively intense (Figure 10.6c). During the later stages, once most of the core is solid, the field is predicted to transition to a multipolar state (which is accompanied by a decrease in intensity), before finally shutting down as solidification completes. The relatively constant field observed in the Imilac corresponds to the strong and stable (i.e. dipolar and non-reversing) period of dynamo activity predicted during the early stages of core solidification. The weakening field observed in the Esquel corresponds to the weaker and more unstable (i.e. multipolar and reversing) regime predicted during the late stage of core solidification. Each region of the CZ captures an average field over a time period of 1–2 Myr. Without higher temporal resolution (e.g. meteorites that cooled more rapidly), it is not possible to distinguish a smooth decrease in the overall dynamo intensity from an increase in the reversal rate of a rapidly reversing field. Both possibilities are

consistent, however, with the predicted behavior during the final stages of a compositionally driven dynamo. The field intensities produced from the model are roughly an order of magnitude less intense than those observed experimentally; we argue that the fields experienced by the Imilac and Esquel meteorite CZs are amplified by deeper mantle-hosted metal, in a similar way to a soft-iron core in a solenoid. The observed intensities are consistent with those obtained independently by Tarduno *et al.* (2012) from the olivine single-crystal paleointensity method.

The direction of core solidification depends principally on the size of a body and the composition of its core (Williams, 2009). Due to their small size and unknown S content, the direction of asteroid core solidification, and hence the ability of asteroids to generate compositionally driven dynamo fields, was previously uncertain. However, with these observations from the pallasites, it is now interesting to consider the types of core convection that may have acted during the early solar system. Calculations of both heat production and core–mantle heat flux suggest that thermally driven convection could only have acted for the first ~10–50 Myr of the solar system (Elkins-Tanton *et al.*, 2011; Sterenborg and Crowley, 2013). On the other hand, compositional convection could only have acted tens to hundreds of millions of years after an asteroid formed, once it had cooled enough for the core to be below its freezing temperature. Hence, initially, an asteroid core may have generated a relatively weak and short-lived thermally driven field. After sufficient cooling, a late-stage, long-lived, and intense period of compositionally driven dynamo activity was likely created among differentiated asteroids that solidified from the bottom up (i.e. by forming an inner core). Owing to the differences in buoyancy created by cooling of the liquid compared to light-element enrichment, compositional convection is a much more efficient mechanism of dynamo generation than thermal convection (Nimmo, 2009). Thus, thermally driven fields were probably sparse, whereas compositionally fields were likely more widespread, resulting in an epoch of magnetic activity among differentiated asteroids that solidified from the bottom up during the early solar system.

10.4 Opportunities for Future Studies

As discussed above, it has largely been assumed that iron meteorites would not have cooled to sufficiently low temperatures to record paleomagnetic information during the period of putative dynamo activity on their parent bodies. However, metallographic cooling rate and siderophile element studies suggest that some iron meteorite parent bodies (e.g. IVA irons) were not covered by a silicate mantle and likely crystallized from the outside inward (Yang *et al.*, 2008; Goldstein *et al.*, 2009b; McCoy *et al.*, 2011), such that the radial temperature gradient on the outside of the body could permit an interior dynamo and a magnetized metallic crust. Such

unmantled bodies are thought to have formed by hit-and-run collisions between differentiated planetesimals, which strip off the overlying silicates while leaving the metallic core largely intact (Asphaug, 2010). Inward core crystallization is permissible given the low internal pressures of asteroid-sized bodies, but is not guaranteed given the poorly known material properties of metallic iron (Williams, 2009) and the fate of solid precipitates (which could form inward-growing dendritic structures or “snow” that sinks into the core; Haack and Scott, 1992). Because some IVA irons also happen to contain silicates that were entrained in their molten metal, they are therefore a prime target for future nanomagnetic analyses of meteoritic metal as well as single silicate crystal paleointensity studies. Given that magnetized iron meteorites would seem to require an unmantled, inwardly crystallizing core, such paleomagnetic studies could directly test the hypotheses of hit-and-run collisions and provide important constraints on the material properties of metallic iron and the style of core crystallization.

10.5 Summary

The dominance of multi-domain kamacite has traditionally lead to the metal component of iron and stony-iron meteorites being dismissed as a reliable carrier of paleomagnetic information. In contrast to this traditional view, we have shown that, under favorable circumstances, paleomagnetic information can be recorded and retained on a local scale within the CZ of meteoritic metal. Furthermore, the developments in synchrotron magnetic imaging now enable the magnetic state of the CZ to be imaged and analyzed quantitatively, opening up new avenues of research into the nanopaleomagnetism of a range of meteorites. Such studies will not only allow us to learn about the thermochemical properties of planetesimals in the early solar system, but provide us with unique opportunities to learn about how magnetic fields are generated on planetary bodies in general, and the underlying physics of the dynamo generation process itself.

Acknowledgments

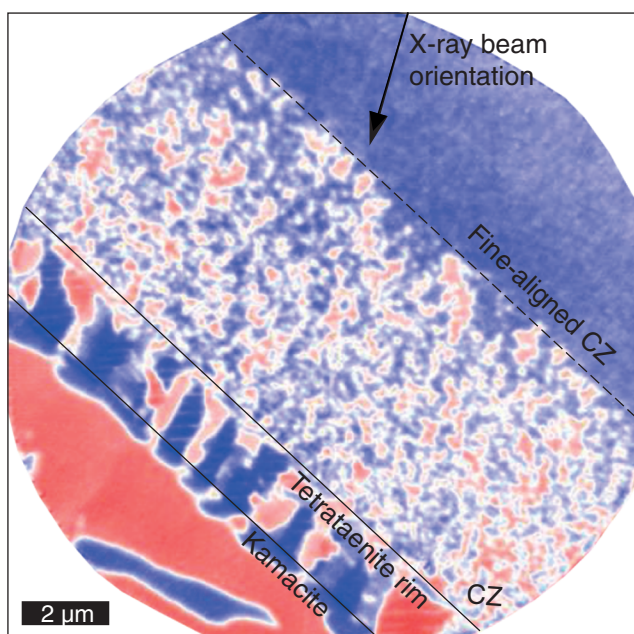
The research leading to these results has received funding from the European Research Council under the European Union’s Seventh Framework Programme (FP/2007–2013)/ERC grant agreement numbers 320750 and 312284, and the Natural Environment Research Council. We thank the Natural History Museum, London, and the Sedgwick Museum of Earth Sciences, University of Cambridge, for samples. We acknowledge our collaborators Julia Herrero-Albillos, Florian Kronast, Takeshi Kasama, Gerrit van der Laan and Francis Nimmo for their contributions to the XPEEM studies and geophysical modeling.

References

- Asphaug, E. 2010. Similar-sized collisions and the diversity of planets. *Chemie der Erde*, **70**, 199–219.
- Asti, G., Solzi, M., Ghidini, M., and Neri, F. 2004. Micromagnetic analysis of exchange-coupled hard–soft planar nanocomposites. *Physical Review B*, **69**, 174401.
- Boesenberg, J. S., Delaney, J. S., and Hewins, R. H. 2012. A petrological and chemical reexamination of main group pallasite formation. *Geochimica et Cosmochimica Acta*, **89**, 134–158.
- Brecher, A. and Albright, L. 1977. The thermoremanence hypothesis and the origin of magnetization in iron meteorites. *Journal of Geomagnetism and Geoelectricity*, **29**, 379–400.
- Bryson, J. F., Church, N. S., Kasama, T., and Harrison, R. 2014a. Nanomagnetic intergrowths in Fe–Ni meteoritic metal: The potential for time-resolved records of planetesimal dynamo fields. *Earth and Planetary Science Letters*, **388**, 237–248.
- Bryson, J. F., Herrero-Albillos, J., Kronast, F., *et al.* 2014b. Nanopaleomagnetism of meteoritic Fe–Ni studied using X-ray photoemission electron microscopy. *Earth and Planetary Science Letters*, **396**, 125–133.
- Bryson, J. F. J., Nichols, C. I. O., Herrero-Albillos, J., *et al.* 2015. Long-lived magnetism from solidification-driven convection on the pallasite parent body. *Nature*, **517**, 472–475.
- Cisowski, S. M. 1987. Magnetism of meteorites. In *Geomagnetism*, ed. J. A. Jacobs. New York: Academic Press, vol. 2, 525–560.
- Clarke, R. S. and Scott, E. R. D. 1980. Tetrataenite – ordered FeNi, a new mineral in meteorites. *American Mineralogist*, **65**, 624–630.
- Dang, M., Dubé, M., and Rancourt, D. 1995. Local moment magnetism of fcc Fe–Ni alloys II. Ising approximation Monte Carlo. *Journal of Magnetism and Magnetic Materials*, **147**, 133–140.
- Dang, M. and Rancourt, D. 1996. Simultaneous magnetic and chemical order-disorder phenomena in Fe₃Ni, FeNi, and FeNi₃. *Physical Review B*, **53**, 2291.
- Dos Santos, E., Gattacceca, J., Rochette, P., Scorzelli, R. B., and Fillion, G. 2014. Magnetic hysteresis properties and ⁵⁷Fe Mössbauer spectroscopy of iron and stony-iron meteorites: Implications for mineralogy and thermal history. *Physics of Earth and Planetary Interiors*, **242**, 50–64.
- Elkins-Tanton, L. T., Weiss, B. P., and Zuber, M. T. 2011. Chondrites as samples of differentiated planetesimals. *Earth and Planetary Science Letters*, **305**, 1–10.
- Fearn, D. R. and Loper, D. E. 1981. Compositional convection and stratification of Earth's core. *Nature*, **289**, 393–394.
- Goldstein, J. and Michael, J. 2006. The formation of plessite in meteoritic metal. *Meteoritics & Planetary Science*, **41**, 553–570.
- Goldstein, J., Scott, E., and Chabot, N. 2009a. Iron meteorites: Crystallization, thermal history, parent bodies, and origin. *Chemie der Erde*, **69**, 293–325.
- Goldstein, J., Yang, J., Kotula, P., Michael, J., and Scott, E. 2009b. Thermal histories of IVA iron meteorites from transmission electron microscopy of the cloudy zone microstructure. *Meteoritics & Planetary Science*, **44**, 343–358.
- Haack, H. and Scott, E. R. D. 1992. Asteroid core crystallization by inward dendritic growth. *Journal of Geophysical Research*, **97**, 14727–14734.
- Hevey, P. J. and Sanders, I. S. 2006. A model for planetesimal meltdown by ²⁶Al and its implications for meteorite parent bodies. *Meteoritics & Planetary Science*, **41**, 95–106.

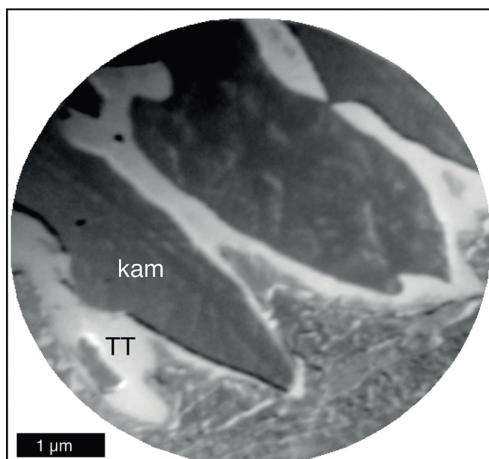
- James, P., Eriksson, O., Johansson, B., and Abrikosov, I. 1999. Calculated magnetic properties of binary alloys between Fe, Co, Ni, and Cu. *Physical Review B*, **59**, 419–430.
- Kleine, T., Touboul, M., Bourdon, B., *et al.* 2009. Hf–W chronology of the accretion and early evolution of asteroids and terrestrial planets. *Geochimica et Cosmochimica Acta*, **73**, 5150–5188.
- Kneller, E. and Hawig, R. 1991. The exchange-spring magnet: a new material principle for permanent magnets. *IEEE Transactions on Magnetics*, **27**, 3588–3600.
- Leroux, H., Doukhan, J.-C., and Perron, C. 2000. Microstructures of metal grains in ordinary chondrites: Implications for their thermal histories. *Meteoritics & Planetary Science*, **35**, 569–580.
- Lewis, L. H., Mubarak, A., Poirier, E., *et al.* 2014. Inspired by nature: Investigating tetraenaite for permanent magnet applications. *Journal of Physics Condensed Matter*, **26**, 064213.
- Locatelli, A. and Bauer, E. 2008. Recent advances in chemical and magnetic imaging of surfaces and interfaces by XPEEM. *Journal of Physics Condensed Matter*, **20**, 093002.
- McCoy, T. J., Walker, R. J., Goldstein, J. I., *et al.*, 2011. Group IVA irons: New constraints on the crystallization and cooling history of an asteroidal core with a complex history. *Geochimica et Cosmochimica Acta*, **75**, 6821–6843.
- Néel, L., Pauleve, J., Pauthenet, R., Laugier, J., and Dautreppe, D. 1964. Magnetic properties of an iron–nickel single crystal ordered by neutron bombardment. *Journal of Applied Physics*, **35**, 873–876.
- Nimmo, F., 2009. Energetics of asteroid dynamos and the role of compositional convection. *Geophysical Research Letters*, **36**, L10201.
- Olson, P. and Christensen, U. R. 2006. Dipole moment scaling for convection-driven planetary dynamos. *Earth and Planetary Science Letters*, **250**, 561–571.
- Rancourt, D., Lagarec, K., Densmore, A., *et al.*, 1999. Experimental proof of the distinct electronic structure of a new meteoritic Fe–Ni alloy phase. *Journal of Magnetism and Magnetic Materials*, **191**, L255–L260.
- Rancourt, D. G. and Scorzelli, R. B. 1995. Low-spin γ -Fe–Ni (γ LS) proposed as a new mineral in Fe–Ni-bearing meteorites: epitaxial intergrowth of γ LS and tetraenaite as a possible equilibrium state at ~ 20 –40 at% Ni. *Journal of Magnetism and Magnetic Materials*, **150**, 30–36.
- Reuter, K. B., Williams, D. B., and Goldstein, J. I. 1988. Low temperature phase transformations in the metallic phases of iron and stony-iron meteorites. *Geochimica et Cosmochimica Acta*, **52**, 617–626.
- Sterenberg, M. G. and Crowley, J. W. 2013. Thermal evolution of early solar system planetesimals and the possibility of sustained dynamos. *Physics of Earth and Planetary Interiors*, **214**, 53–73.
- Tarduno, J. A., Cottrell, R. D., Nimmo, F., *et al.*, 2012. Evidence for a dynamo in the main group pallasite parent body. *Science*, **338**, 939–42.
- Tarduno, J. A., Cottrell, R., Watkeys, M., *et al.* 2010. Geodynamo, solar wind, and magnetopause 3.4 to 3.45 billion years ago. *Science*, **327**, 1238–1240.
- Uehara, M., Gattacceca, J., Leroux, H., Jacob, D., and van der Beek, C. J. 2011. Magnetic microstructures of metal grains in equilibrated ordinary chondrites and implications for paleomagnetism of meteorites. *Earth and Planetary Science Letters*, **306**, 241–252.
- Wasilewski, P. 1988. Magnetic characterization of the new magnetic mineral tetraenaite and its contrast with isochemical taenite. *Physics of Earth and Planetary Interiors*, **52**, 150–158.

- Wasson, J. T. and Choi, B.-G. 2003. Main-group pallasites: Chemical composition, relationship to IIIAB irons, and origin. *Geochimica et Cosmochimica Acta*, **67**, 3079–3096.
- Weiss, B. P., Berdahl, J. S., Elkins-Tanton, L., *et al.*, 2008. Magnetism on the angrite parent body and the early differentiation of planetesimals. *Science*, **322**, 713–716.
- Williams, Q. 2009. Bottom-up versus top-down solidification of the cores of small solar system bodies: Constraints on paradoxical cores. *Earth and Planetary Science Letters*, **284**, 564–569.
- Yang, C., Williams, D., and Goldstein, J. 1996. A revision of the Fe–Ni phase diagram at low temperatures (< 400 °C). *Journal of Phase Equilibria*, **17**, 522–531.
- Yang, C.-W., Williams, D. B., and Goldstein, J. I. 1997a. Low-temperature phase decomposition in metal from iron, stony-iron, and stony meteorites. *Geochimica et Cosmochimica Acta*, **61**, 2943–2956.
- Yang, C., Williams, D. B., and Goldstein, J. I. 1997b. A new empirical cooling rate indicator for meteorites based on the size of the cloudy zone of the metallic phases. *Meteoritics & Planetary Science*, **32**, 423–429.
- Yang, J., Goldstein, J. I., and Scott, E. R. 2010. Main-group pallasites: Thermal history, relationship to IIIAB irons, and origin. *Geochimica et Cosmochimica Acta*, **74**, 4471–4492.
- Yang, J., Goldstein, J. I., and Scott, E. R. D. 2008. Metallographic cooling rates and origin of IVA iron meteorites. *Geochimica et Cosmochimica Acta*, **72**, 3043–3061.
- Zhang, J., Williams, D., and Goldstein, J. 1993. The microstructure and formation of duplex and black plessite in iron meteorites. *Geochimica et Cosmochimica Acta*, **57**, 3725–3735.

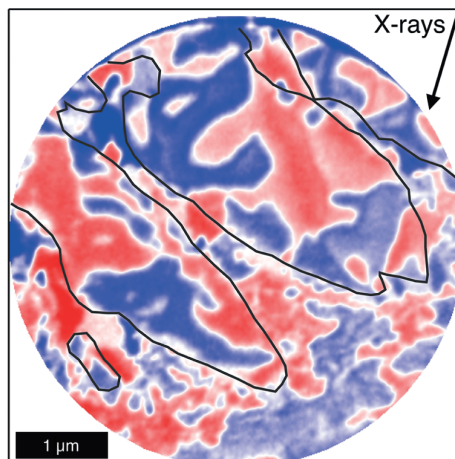


For caption, see figure 10.2 in the main text.

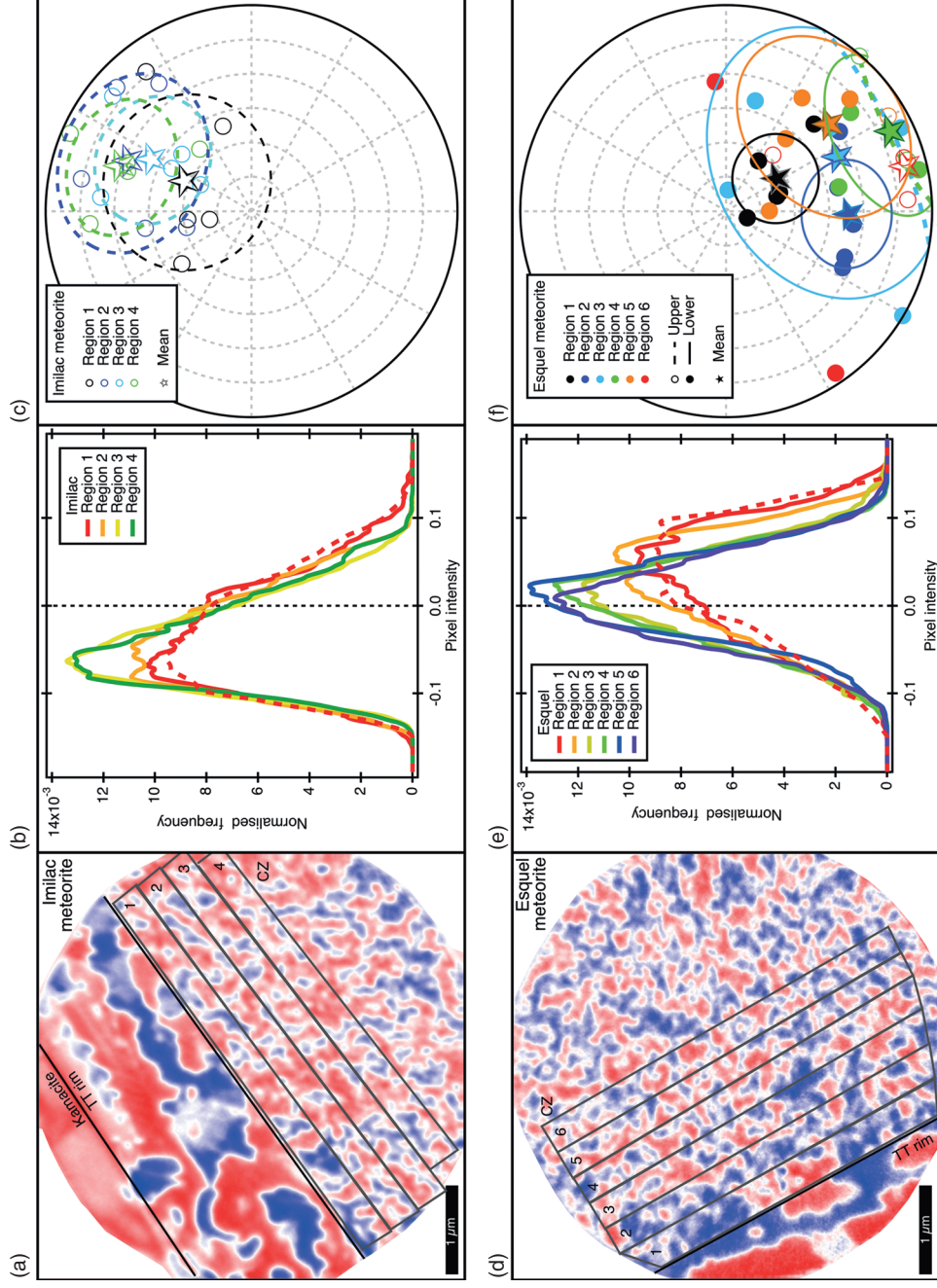
(a)



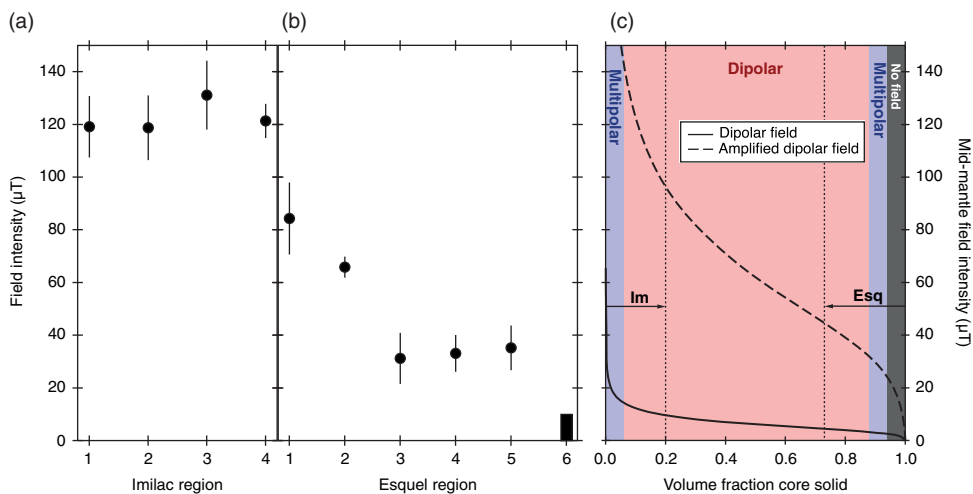
(b)



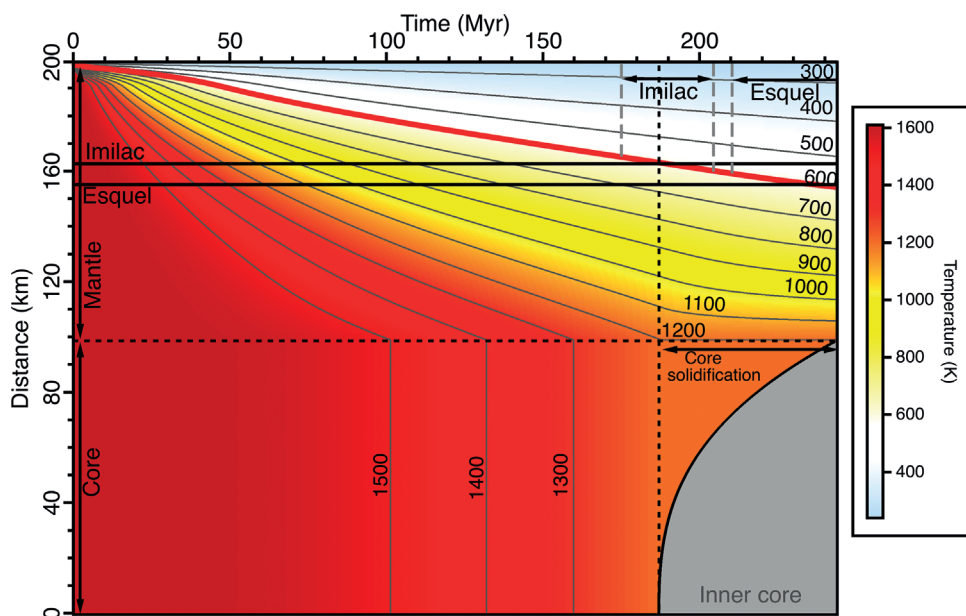
For caption, see figure 10.3 in the main text.



For caption, see figure 10.5 in the main text.



For caption, see figure 10.6 in the main text.



For caption, see figure 10.7 in the main text.